Nanoscale

COMMUNICATION

View Article Online
View Journal | View Issue

Cite this: *Nanoscale*, 2022, **14**, 2599

Received 20th December 2021,
Accepted 20th January 2022

DOI: 10.1039/d1nr08350c

rsc.li/nanoscale

Size-dependent flame retardancy of black phosphorus nanosheets†

Zunbin Duan, [a,b] Yanfang Wang,[a,c] Shi Bian,[a] Danni Liu,[a] Yanli Zhang,[a] Xue Zhang,[a] Rui He,*[a] Jiahong Wang, *[a] Guangbo Qu,*[b] Paul K. Chu [d] and Xue-Feng Yu [a]

Two-dimensional black phosphorus (BP) nanosheets are potential flame-retardant nano-additives. Herein, the effects of the size of BP nanosheets embedded in epoxy resin (EP) on flame retardancy are studied. BP nanosheets with four different sizes are synthesized from bulk BP by different exfoliation methods including solid ball milling, liquid ball milling, ultrasonic liquid exfoliation, and electrochemical exfoliation (samples are designated as sb-BP, lb-BP, us-BP, and ec-BP, respectively). lb-BP exhibits the best dispersion in the EP matrix, and the lb-BP/EP composite shows the best flame-retardancy properties among the four BP/EP composites. Compared to bare EP, lb-BP/EP shows obvious improvements including the reduction in the heat release peak rate by 34.4%, total heat release by 27.0%, peak of smoke production rate by 69.2%, and total production of carbon monoxide by 50.8%. The mechanistic study reveals that lb-BP serves as a barrier and carbonization catalyst to delay combustion. These results confirm the size dependence of flame-retardancy properties of BP nanosheets and the new knowledge provides insights into the size dependent effects of other two-dimensional materials.

1. Introduction

Black phosphorus (BP) as a burgeoning class of two-dimensional (2D) materials has attracted wide attention in recent years.[1–3] The phosphorus atom in BP bonds with three adjacent atoms in the single orthorhombic puckered layer.[2,4] Owing to the unique 2D morphology and best thermodynamic stability among phosphorus allotropes, BP nanosheets exfoliated from bulk BP have recently been proposed as flame-retardant nano-additives[2,5–7] on the heels of the discovery of flame retardancy of traditional micro-size red phosphorus.[8,9] So far, investigations of BP-based flame-retardant additives have mainly focused on surface modifications and progress has been made to improve the affinity between BP and the matrix.[5,10–12] The geometric characteristics are one of the fundamental and important factors of flame-retardant additives[13–16] as they impact the dispersion of inorganic nano-additives in the matrix and consequently the effectiveness.[13,16,17] However, there have been few studies on the effects of the size of BP nanosheets on the flame-retardancy characteristics.

BP nanosheets are mainly prepared by top-down exfoliation techniques such as mechanical cleavage,[1,18] solid ball milling,[19,20] liquid ball milling,[21,22] ultrasonic liquid exfoliation,[23–25] high-speed shearing,[26] and electrochemical exfoliation[27–29] and different methods yield different morphologies. Mechanical cleavage is employed to exfoliate clean nanosheets with outstanding physical properties, but the productivity and yield are relatively poor.[1,30] Ball milling usually induces high stress and the bulk crystals tend to be broken into pieces with a small lateral size and relatively thick morphology.[31,32] Ultrasonic and high-speed shearing are two common exfoliation methods to prepare thin nanosheets with a diameter of hundreds of nanometers[3,33] and electrochemical intercalation is the preferred technique to prepare atomically thin and micrometer-sized sheets in a scalable fashion.[28,29,34] In fact, large-scale production of BP nanosheets depends on the synthesis techniques, which also impact the flame-retardancy properties of BP nanosheets.

Herein, four types of BP nanosheets with different lateral lengths and thicknesses are prepared by four different techniques of solid ball milling, liquid ball milling, ultrasonic exfo-

[a]*Shenzhen Engineering Center for the Fabrication of Two-Dimensional Atomic Crystals, Shenzhen Institute of Advanced Technology, Chinese Academy of Sciences, Shenzhen 518055, China. E-mail: jh.wang1@siat.ac.cn, rui.he1@siat.ac.cn*
[b]*State Key Laboratory of Environmental Chemistry and Ecotoxicology, Research Center for Eco-Environmental Sciences, Chinese Academy of Sciences, Beijing 100085, China. E-mail: gbqu@rcees.ac.cn*
[c]*Heilongjiang Key Laboratory of Molecular Design and Preparation of Flame Retarded Materials, College of Chemistry, Chemical Engineering and Resource Utilization, Northeast Forestry University, Harbin, 150040, China*
[d]*Department of Physics, Department of Materials Science and Engineering, and Department of Biomedical Engineering, City University of Hong Kong, Tat Chee Avenue, Kowloon, Hong Kong, China*

†Electronic supplementary information (ESI) available: Experimental methods, calculations and ESI figures and tables. See DOI: 10.1039/d1nr08350c

liation, and electrochemical intercalation. The BP nanosheets are dispersed in epoxy resin (EP) to form BP/EP composites to compare the size dependent flame-retardancy properties. Our results disclose that BP nanosheets prepared by liquid ball milling show the most uniform dispersion in the EP matrix as well as the best flame retardancy. The underlying mechanism is investigated and proposed.

2. Results and discussion

The BP nanosheets with different sizes are prepared by exfoliating bulk BP *via* four techniques, namely solid ball milling, liquid ball milling, ultrasonic exfoliation, and electrochemical intercalation (Fig. 1a) and the samples are designated as sb-BP, lb-BP, us-BP, and ec-BP, respectively. The lateral thicknesses and diameters of the BP nanosheets are measured by atomic force microscopy (AFM) and scanning electron microscopy (SEM). As shown in Fig. 1b, c and S1,† the average thicknesses of sb-BP, lb-BP, us-BP, and ec-BP are 91.8 ± 20.1 nm, 45.4 ± 12.1 nm, 20.5 ± 4.2 nm, and 8.2 ± 2.1 nm, respectively. According to the SEM images and statistics (Fig. 1d, e and S2†), the average diameters of sb-BP, lb-BP, us-BP, and ec-BP are 201 ± 58 nm, 639 ± 143 nm, 244 ± 42 nm, and 865 ± 262 nm, respectively.

The structure of the BP nanosheets is analyzed by powder X-ray diffraction (XRD), Raman scattering, and transmission electron microscopy (TEM). As shown in Fig. S3,† the XRD patterns of the four BP nanosheets can be indexed to the orthorhombic phase of the bulk BP crystals. The small signal-to-noise ratios of sb-BP and lb-BP indicate that ball milling partially destroys the crystallinity of BP. As shown in Fig. S4,† the three peaks at 360.6 cm^{-1}, 439.7 cm^{-1}, and 466.2 cm^{-1} correspond to the vibrational modes of A_g^1, B_{2g}, and A_g^2 of BP[35] thus corroborating structural integrity. The TEM image shown in Fig. S5† reveals that the structure of the lb-BP nanosheets is intact. The chemical composition of the BP nanosheets is determined by X-ray photoelectron spectroscopy (XPS) as shown in Fig. S6.† The P 2p peak can be fitted by three peaks corresponding to P $2p_{3/2}$ (*ca.* 130.0 eV), P $2p_{1/2}$ (*ca.* 130.6 eV), and P–O (*ca.* 134.0 eV).[36,37] The low intensity of the P–O peak near 134.0 eV indicates a small degree of oxidation of the BP nanosheets.

Since the dispersion characteristics of the BP nanosheets in the EP matrix affect the properties of the composites,[38,39] different BP nanosheets with the same concentration (1.0 wt%) are dispersed in the EP matrix. The SEM images of the freeze-fractured cross-section of the BP/EP composites are acquired and analyzed. Since the nanosheet additive alters the mechanical properties of EP, it is generally believed that a rougher and more wrinkled fractured surface indicates more uniform dispersion of the nanosheets in the matrix.[40,41] As shown in the SEM images obtained at different magnifications (Fig. 2a–c), the four BP/EP composites have rough fracture surfaces with different degrees of corrugations and protrusions compared to bare BP. Among the four composites, lb-BP/EP

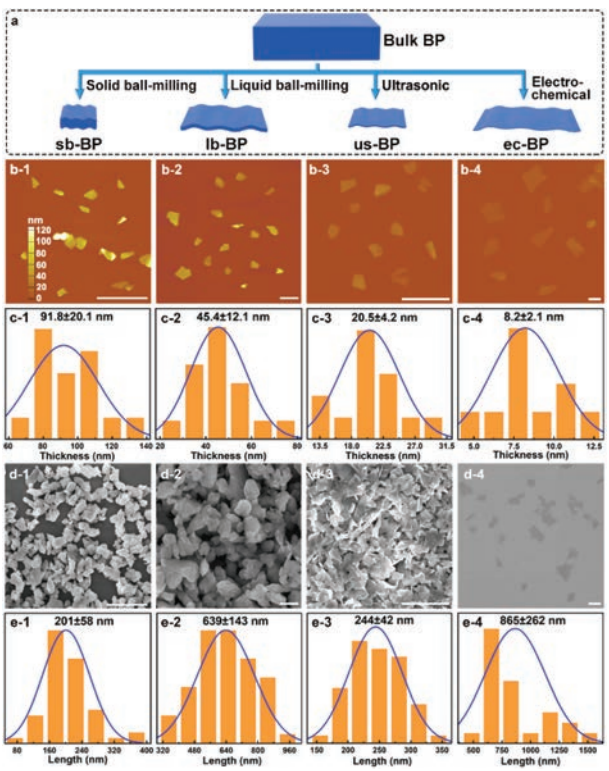

Fig. 1 Synthesis and characterization of BP nanosheets with different sizes: (a) schematic illustration of the synthesis of BP nanosheets; (b) AFM images of (b-1) sb-BP, (b-2) lb-BP, (b-3) us-BP, and (b-4) ec-BP; (c) thickness distributions of the BP nanosheets in Fig. 1b; (d) SEM images of (d-1) sb-BP, (d-2) lb-BP, (d-3) us-BP, and (d-4) ec-BP; and (e) length distributions of the BP nanosheets in Fig. 1d. All the scale bars are 1 μm.

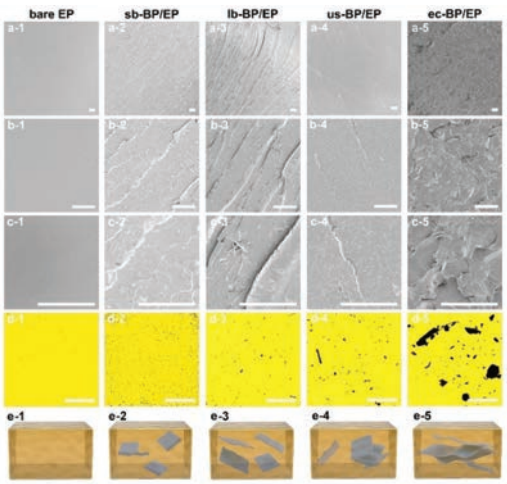

Fig. 2 Dispersion properties of the BP nanosheets in EP: (a–c) SEM images of the freeze-fractured surfaces of the bare EP and different BP/EP composites; (d) optical micrographs of the bare EP and BP/EP composites; (e) possible structures of the four BP/EP composites and bare EP. All the scale bars are 20 μm.

exhibits the roughest fractured surface. No obvious block structure is observed in the fracture surfaces except for ec-BP/EP. In the optical micrographs (Fig. 2d), lb-BP/EP shows the least number of black dots confirming the best dispersion effects. Based on SEM and optical microscopy, the order of the degree of dispersion is: lb-BP > sb-BP > us-BP > ec-BP (Fig. 2e). The difference can be attributed to the different interface compatibility between the BP nanosheets and the EP matrix. By using different synthesis techniques, the size of the BP nanosheets and BP-EP interfacial interactions can be regulated to adjust the extent of re-aggregation. The results disclose that the dispersion of BP in the EP matrix can be improved by selecting a suitable synthesis technique and lb-BP shows the best uniformity.

The thermal stability of the composites is evaluated by thermogravimetric analysis under nitrogen (Fig. S7†). All four BP/EP composites exhibit rapid mass losses at 300–450 °C, but the maximum mass loss rates are different. The lb-BP/EP fares the best, for instance, 11.3 wt% residual weight at 800 °C and 1.1% $°C^{-1}$ maximum weight loss rate. During thermal decomposition, the BP nanosheets act as a barrier to partially prevent diffusion of volatile pyrolytic products and promote catalytic carbonization consequently improving the thermal stability.[2,7] The good thermal stability of lb-BP/EP suggests that lb-BP with the appropriate nano-scale size produces the best barrier and catalytic carbonization effects among the four BP nanosheets.

The flame retardancy of the BP/EP composites and bare EP is evaluated by the flammability test and cone calorimetry. As shown in Fig. 3a-1, all the BP/EPs are burned slowly compared to the bare EP, in which the fire of lb-BP/EP is the smallest during combustion. The residual weight after the decomposition of lb-BP/EP is up to 16.6%, which is the maximum amount among the five residual weights (Fig. 3a-2). Therefore, it is preliminarily judged that the lb-BP nanosheets possess the best flame retardancy.

Heat release, smoke generation, and evolution of toxic carbon monoxide (CO) are investigated by cone calorimetry.[42] Fig. 3b shows the heat release rate (HRR) and total heat release (THR). Bare EP shows large peaks of HRR (pHRR) and THR. On the other hand, pHRR and THR of the four BP/EP composites decrease by different degrees. The corresponding parameters of lb-BP/EP are the smallest among the four BP/EP composites, for instance, the decrease of pHRR and THR by 34.4% and 27.0%, respectively, indicating that the addition of BP nanosheets with the appropriate size reduces heat release. The smoke production rate (SPR) and total smoke production (TSP) of BP/EPs and bare EP are shown in Fig. 3c. Owing to polycyclic aromatic hydrocarbons in EP, when EP is burnt, a large amount of smoke is released. The four BP/EPs with different BP sizes show smaller SPR and TSP than bare EP. This is because the BP nanosheets delay the release of volatile species to hinder further combustion of the BP/EPs inside. Among the four BP/EP composites, lb-BP/EP shows reduction

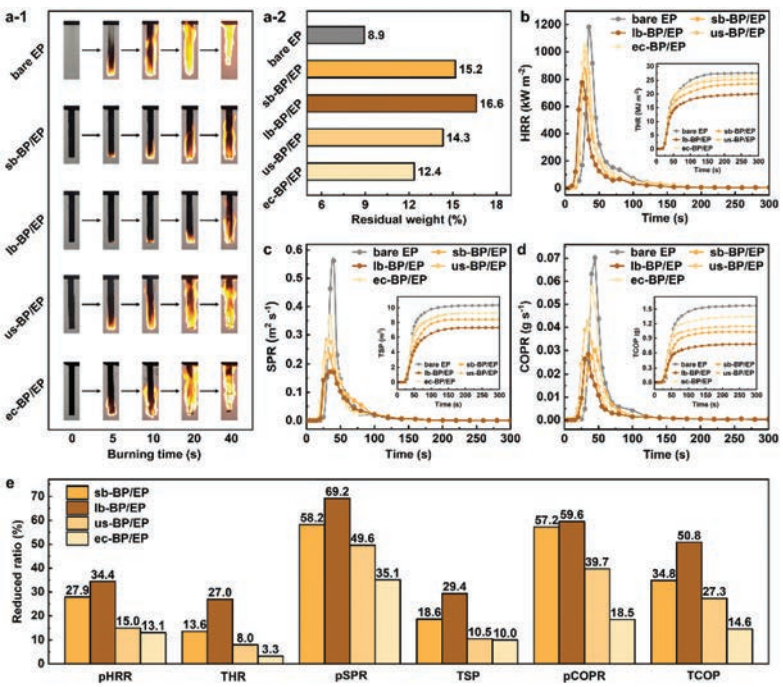

Fig. 3 Flame retarding characteristics of different BP/EP composites: (a) combustion of the four BP/EPs and bare EP: (a-1) photographs of the combustion and (a-2) residual weight after decomposition; (b–d) heat release, smoke generation and CO production in cone calorimetry: (b) HRR with the inset of THR, (c) SPR with the inset of TSP, and (d) COPR with the inset of TCOP curves; (e) reduction ratios of the burning parameters in cone calorimetry.

ratios of the SPR peak (pSPR) and TSP of up to 69.2% and 29.4%, respectively.

CO is the main toxic substance that evolves during combustion and reducing the release rate and amount of CO is crucial. As shown in Fig. 3d, the CO release rates and amounts observed from the four BP/EPs are obviously less than those from the bare EP. Among the four BP/EPs, lb-BP/EP again delivers the best performance as exemplified by the reduction of CO production rate peak (pCOPR) and total CO production (TCOP) by 59.6% and 50.8%, respectively. The detailed results are summarized in Fig. 3e and Table S1.† The decrease in infrared absorption intensity observed from lb-BP/EP is the largest, indicating that lb-BP/EP generates the least amount of organic gases during decomposition (Fig. S8†).

The amount of residual carbon is determined by cone calorimetry. The compact and continuous carbon layer delays heat transfer and release of volatile combustion products to enhance fire resistance.[43] Fig. 4a shows the photographs of the residual carbon on the bare EP and four BP/EP composites. Some amount of residual carbon is found from the bare EP, whereas more and denser residual carbon is present on the BP/EP composites after combustion. The microstructure of the residual carbon is analyzed by SEM (Fig. 4b). Compared to the thin residual carbon layer on the bare EP, denser and thicker residual carbon exists on the four BP/EP composites, suggesting that BP nanosheets improve the quality of residual carbon.

The residual carbon layer with a high graphitization degree is likely to act as a barrier which would lead to a lower oxygen environment to mitigate burning. As shown in Fig. 4c, the residual carbon diffraction peaks from lb-BP/EP and sb-BP/EP are close to 2θ of 26°. Since the main diffraction peak from the (002) crystal plane of graphite is at 26°, the formation of graphitized carbon is indicated and the similarity suggests a high degree of graphitization.[5,44] In addition, the characteristic peaks of BP disappeared, implying that the BP nanosheets decompose during combustion. A similar conclusion can be drawn from the Raman spectra in Fig. 4d and S9.† The two peaks at 1365 cm^{-1} and 1596 cm^{-1} represent the D and G peaks of graphite, respectively,[45,46] and the ratio (I_D/I_G) reflects the extent of graphitization. As a smaller I_D/I_G indicates more graphitization[5] and lb-BP/EP and sb-BP/EP show smaller I_D/I_G ratios (2.02 and 2.11) than the bare EPs (3.24) or other two BP/EPs, better graphitization can be inferred.

The XPS survey spectrum in Fig. S10† shows that the residual carbon on lb-BP/EP is mainly composed of P, O, C, and N. The P 2p peak is composed of three peaks at 133.5 eV, 134.3 eV and 135.0 eV associated with P═O, P–O, and P_2O_5, respectively (Fig. 4e), revealing the formation of phosphorus oxide and phosphoric acid derivatives which can promote the formation of char and delay burning, which is confirmed by the O 1s XPS spectrum shown in Fig. 4f.

Based on these results, the flame retarding mechanism is postulated as shown in Fig. 5. Owing to the moderate size, the lb-BP nanosheets are dispersed well in the EP matrix and self-aggregation can be avoided. Before decomposition, the 2D nanosheets act as a barrier against the evolution of volatile

Fig. 5 Size-dependent flame retarding mechanism of BP/EPs.

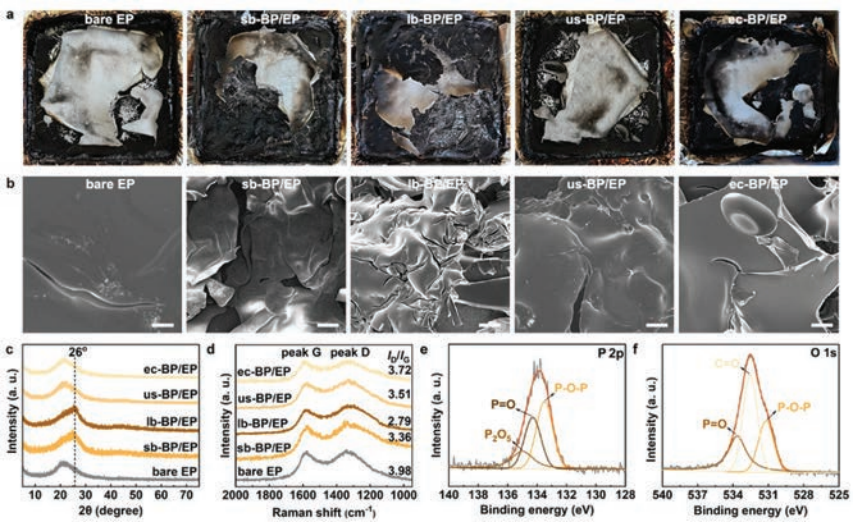

Fig. 4 Analysis of the residual carbon after combustion: (a) photographs, (b) SEM images, (c) XRD patterns, and (d) Raman scattering spectra of the residual carbons on bare EP and BP/BPs. (e) P 2p and (f) O 1s XPS spectra of the residual carbon on lb-BP/BP. The scale bars in Fig. 4b are 50 μm.

combustion products and heat generation. During decomposition, lb-BP facilitates the formation of a dense carbon layer that delays heat and mass transfer to the outside and improves the flame retardancy of lb-BP/EP. With respect to the other three BP/EP composites containing BP nanosheets of different sizes, the poorer dispersion characteristics give rise to worse flame-retardancy properties. The fire retarding properties of lb-BP/EP are compared to those of previously reported BP-based composites and are shown in Table S2,† the liquid ball milled and exfoliated BP nanosheets have the best properties. The results demonstrate that the optimal size and appropriate synthesis technique are critical to flame retardancy. Moreover, because the liquid ball milling exfoliation method is scalable (Fig. S11†), it bodes well for industrial mass production.

3. Conclusions

BP nanosheets with different sizes are prepared from bulk BP crystals by different exfoliation methods and the size-dependent flame retardancy is evaluated. The lb-BP nanosheets produced by liquid ball milling exfoliation have the optimal size with a lateral diameter of 640 nm and a thickness of 45 nm, thus facilitating uniform dispersion in the EP matrix and producing the best flame-retardant properties. Compared to the bare EP, all the pertinent fire retarding properties of lb-BP/EP are better, for instance, the reduction of pHRR, THR, pSPR, TSP, pCOPR, and TCOP by 34.4%, 27.0%, 69.2%, 29.4%, 59.6%, and 50.8%, respectively. The lb-BP nanosheets with a medium size not only act as a barrier, but also catalyze carbonization to delay the combustion of the lb-BP/EP composite. This study reveals the importance of particle size in the flame retardancy of BP nanosheets as well as the dispersion of the nanomaterials in the matrix. The liquid ball milling exfoliation method which delivers the best performance can be readily scaled up for mass production of other types of 2D nanomaterials to cater to industrial demand.

Author contributions

X.-F. Yu, G. B. Qu, J. H. Wang and R. He conceived the project and supervised the study. Z. B. Duan and Y. F. Wang performed most of the experiments. S. Bian, Y. F. Wang, D. N. Liu, and Y. L. Zhang assisted in the characterization work. Z. B. Duan, J. H. Wang, S. Bian, X.-F. Yu, G. B. Qu, and R. He discussed the data. Z. B. Duan, J. H Wang, G. B. Qu, R. He, X. Zhang, X.-F. Yu and P. K. Chu co-wrote the manuscript.

Conflicts of interest

The authors declare no competing interest.

Acknowledgements

This work was financially supported by the National Natural Science Foundation of China (21975280, 21908238, and 22102208), the Youth Innovation Promotion Association Chinese Academy of Sciences (2020354), the China Postdoctoral Science Foundation (2021M703367), the Guangdong Provincial Natural Science Foundation (2020A1515010380, 2019A1515111062, 2020A1515110378, and 2020A1515110831), the Shenzhen Science and Technology Research Funding (JCYJ20180507182530279 and JCYJ20180507182047316), and the City University of Hong Kong Strategic Research Grant (7005505).

References

1 L. Li, Y. Yu, G. J. Ye, Q. Ge, X. Ou, H. Wu, D. Feng, X. H. Chen and Y. Zhang, *Nat. Nanotechnol.*, 2014, **9**, 372–377.
2 G. Qu, T. Xia, W. Zhou, X. Zhang, H. Zhang, L. Hu, J. Shi, X. Yu and G. Jiang, *Chem. Rev.*, 2020, **120**, 2288–2346.
3 X. Chen, J. S. Ponraj, D. Fan and H. Zhang, *Nanoscale*, 2020, **12**, 3513–3534.
4 Y. Sui, J. Zhou, X. Wang, L. Wu, S. Zhong and Y. Li, *Mater. Today*, 2021, **42**, 117–136.
5 S. Qiu, Y. Zhou, X. Zhou, T. Zhang, C. Wang, R. K. K. Yuen, W. Hu and Y. Hu, *Small*, 2019, **15**, 1805175.
6 X. Ren, Y. Mei, P. Lian, D. Xie, Y. Yang, Y. Wang and Z. Wang, *Polymers*, 2018, **10**, 227.
7 Y. Zhang, C. Ma, J. Xie, H. ågren and H. Zhang, *Adv. Mater.*, 2021, **33**, 2100113.
8 Y. Zhou, J. Huang, J. Wang, F. Chu, Z. Xu, W. Hu and Y. Hu, *Polym. Degrad. Stab.*, 2020, **178**, 109194.
9 Y. Xiao, J. Li, J. Wu, L. Song, Y. Han, Z. Wang and Q. Yu, *Polym. Adv. Technol.*, 2021, **32**, 3515–3522.
10 S. Qiu, Y. Zhou, X. Ren, B. Zou, W. Guo, L. Song and Y. Hu, *Chem. Eng. J.*, 2020, **402**, 126212.
11 W. Cai, T. Cai, L. He, F. Chu, X. Mu, L. Han, Y. Hu, B. Wang and W. Hu, *J. Hazard. Mater.*, 2020, **387**, 121971.
12 S. Yin, X. Ren, P. Lian, Y. Zhu and Y. Mei, *Polymers*, 2020, **12**, 1487.
13 X. Yue, C. Li, Y. Ni, Y. Xu and J. Wang, *J. Mater. Sci.*, 2019, **54**, 13070–13105.
14 N. A. Isitman, M. Dogan, E. Bayramli and C. Kaynak, *Polym. Degrad. Stab.*, 2012, **97**, 1285–1296.
15 Y. Liu, J. Li and Q. Wang, *J. Appl. Polym. Sci.*, 2009, **113**, 2046–2051.
16 L. Yan, Z. Xu and J. Zhang, *J. Therm. Anal. Calorim.*, 2017, **130**, 1987–1996.
17 H. Huang, M. Tian, L. Liu, W. Liang and L. Zhang, *J. Appl. Polym. Sci.*, 2006, **100**, 4461–4469.
18 H. Liu, A. T. Neal, Z. Zhu, Z. Luo, X. Xu, D. Tománek and P. D. Ye, *ACS Nano*, 2014, **8**, 4033–4041.
19 S. Thurakkal, D. Feldstein, R. Perea-Causín, E. Malic and X. Zhang, *Adv. Mater.*, 2021, **33**, 2005254.

20 X. Zhu, T. Zhang, Z. Sun, H. Chen, J. Guan, X. Chen, H. Ji, P. Du and S. Yang, *Adv. Mater.*, 2017, **29**, 1605776.
21 D. K. Sang, H. Wang, Z. Guo, N. Xie and H. Zhang, *Adv. Funct. Mater.*, 2019, **29**, 1903419.
22 W. Liu, Y. Zhu, X. Xu, S. Wang and X. Zhang, *J. Mater. Sci.: Mater. Electron.*, 2020, **31**, 9543–9549.
23 L. Wu, J. Wang, J. Lu, D. Liu, N. Yang, H. Huang, P. K. Chu and X. Yu, *Small*, 2018, **14**, 1801405.
24 Y. Zhao, H. Wang, H. Huang, Q. Xiao, Y. Xu, Z. Guo, H. Xie, J. Shao, Z. Sun, W. Han, X. Yu, P. Li and P. K. Chu, *Angew. Chem., Int. Ed.*, 2016, **55**, 5003–5007.
25 V. Sresht, A. A. H. Pádua and D. Blankschtein, *ACS Nano*, 2015, **9**, 8255–8268.
26 F. Xu, B. Ge, J. Chen, A. Nathan, L. L. Xin, H. Ma, H. Min, C. Zhu, W. Xia and Z. Li, *2D Mater.*, 2016, **3**, 25005.
27 A. Ambrosi, Z. Sofer and M. Pumera, *Angew. Chem., Int. Ed.*, 2017, **56**, 10443–10445.
28 D. Liu, J. Wang, S. Bian, Q. Liu, Y. Gao, X. Wang, P. K. Chu and X. F. Yu, *Adv. Funct. Mater.*, 2020, **30**, 2002731.
29 Y. Yang, H. Hou, G. Zou, W. Shi, H. Shuai, J. Li and X. Ji, *Nanoscale*, 2018, **11**, 16–33.
30 B. Jayasena and S. Subbiah, *Nanoscale Res. Lett.*, 2011, **6**, 95.
31 H. Zhao, J. H. Kwak, Y. Wang, J. A. Franz, J. M. White and J. E. Holladay, *Energy Fuels*, 2006, **20**, 807–811.
32 C. C. Piras, S. Fernández-Prieto and W. M. De Borggraeve, *Nanoscale Adv.*, 2019, **1**, 937–947.
33 C. Cai, N. Sang, Z. Shen and X. Zhao, *J. Exp. Nanosci.*, 2017, **12**, 247–262.
34 Y. Zhang and Y. Xu, *Adv. Funct. Mater.*, 2019, **29**, 1902171.
35 H. B. Ribeiro, M. A. Pimenta and C. J. S. de Matos, *J. Raman Spectrosc.*, 2018, **49**, 76–90.
36 M. T. Edmonds, A. Tadich, A. Carvalho, A. Ziletti, K. M. O. Donnell, S. P. Koenig, D. F. Coker, B. özyilmaz, A. H. C. Neto and M. S. Fuhrer, *ACS Appl. Mater. Interfaces*, 2015, **7**, 14557–14562.
37 S. Qiu, Y. Zhou, X. Ren, B. Zou, W. Guo, L. Song and Y. Hu, *Chem. Eng. J.*, 2020, **402**, 126212.
38 E. Reynaud, T. Jouen, C. Gauthier, G. Vigier and J. Varlet, *Polymer*, 2001, **42**, 8759–8768.
39 T. Tasaki, Y. Guo, H. Machida, S. Akasaka and A. Fujimori, *Polym. Compos.*, 2019, **40**(S1), E842.
40 S. Qiu, B. Zou, T. Zhang, X. Ren, B. Yu, Y. Zhou, Y. Kan and Y. Hu, *Chem. Eng. J.*, 2020, **401**, 126058.
41 Z. Qu, K. Wu, E. Jiao, W. Chen, Z. Hu, C. Xu, J. Shi, S. Wang and Z. Tan, *Chem. Eng. J.*, 2020, **382**, 122991.
42 S. Nazaré, B. Kandola and A. R. Horrocks, *Fire Mater.*, 2002, **26**, 191–199.
43 I. van der Veen and J. de Boer, *Chemosphere*, 2012, **88**, 1119–1153.
44 H. Bian, A. Kan, Z. Yao, Z. Duan, H. Zhang, S. Zhang, L. Zhu and D. Xia, *J. Phys. Chem. C*, 2019, **123**, 29543–29555.
45 A. C. Ferrari, *Solid State Commun.*, 2007, **143**, 47–57.
46 L. G. Cançado, K. Takai, T. Enoki, M. Endo, Y. A. Kim, H. Mizusaki, N. L. Speziali, A. Jorio and M. A. Pimenta, *Carbon*, 2008, **46**, 272–275.